International Journal of Theoretical Physics, Vol. 42, No. 5, May 2003 (© 2003)

Geometry and Topology Induced Electronic Properties of Graphene Derived Quantum Systems

M. Szopa,[1] M. Margańska, and E. Zipper

Received April 9, 2003

Three different topological structures built on the basis of a graphene lattice are investigated. Clusters of the (3,6) type homeomorphic with the sphere, toroidal, and cylindrical carbon nanotubes are shown to have the same dispersion relation, inherited from the planar graphene lattice. The persistent currents in axially symmetric structures, their dependence on the size and geometry of the molecule, are also discussed.

KEY WORDS: carbon cages; nanotubes; electronic properties; persistent currents.

1. INTRODUCTION

Since the discovery of fullerenes and carbon nanotubes (Ijima, 1991; Krato *et al.*, 1985) there has been an ongoing experimental and theoretical effort (e.g., Dresselhaus *et al.*, 2001; Fowler *et al.*, 2000; Gonzalez *et al.*, 1993) to understand their electronic and magnetic properties. Our approach to this problem is to exploit the information given by the topology of various carbon clusters to derive their energy spectra, which determine the cluster's electronic and magnetic properties.

By applying different boundary conditions to the graphene planes, one can form different convex ploy hedral structures, such as tetrahedral cages (regular and irregular), carbon tori, and nanotubes. The momentum distributions thus obtained differ according to the topology of the cage.

When the tori or carbon nanotubes are inserted into an external static magnetic field parallel to their cylindrical symmetry axis, and as a result persistent nondissipative currents (Cheung *et al.*, 1988) run along the circumference of the structure. These currents are one of the manifestations of quantum coherence.

Using this particular approach we illustrate the role played by topology in such quantum systems.

[1] To whom correspondence should be addressed at . . . ; e-mail: szopa@plktusll.bitnet.

0020-7748/03/0500-1119/0 © 2003 Plenum Publishing Corporation

2. THE CLASSIFICATION OF CONVEX TRIVALENT CAGES

Let us consider a molecule consisting of a set of atoms forming a trivalent and convex polyhedral cage. The trivalent means that each atom is bound to its three nearest neighbors. The simplest possible cage of that type is the set of four atoms in vertices of a tetrahedron. The topological theorem useful for classifying all possible cages of that type is the Euler–Poincaré theorem, which for convex (and therefore homeomorphic with the sphere) cages reads as follows.

Theorem 2.1. *(Euler–Poincaré). For any polyhedron P:*

$$V - E + F = 2, \tag{1}$$

where V is the number of vertices, E – the number of edges, and F – the number of faces of the polyhedron.

For our trivalent lattice, the number of edges $E = 3V/2$ (because each edge belongs to two vertices) and, therefore, $F = 2 + V/2$. Assuming that we have n_l, l-gonal faces the total number of faces and vertices are respectively:

$$F = \sum_l n_l \quad \text{and} \quad V = \frac{1}{3}\sum_l l n_l, \tag{2}$$

where summation goes over all types of l-gonal faces. The Euler–Poincaré theorem yields then the following rule that must hold for any trivalent and convex cage (Szopa, 2001)

$$\sum_l n_l \left(1 - \frac{l}{6}\right) = 2. \tag{3}$$

The same rule can be obtained from the geometrical Gauss–Bonnet theorem, which states

$$\sum_l n_l \gamma_l = 4\pi, \tag{4}$$

where γ_l is the vertex defect connected with the l-gonal face of the polyhedron. Let us start our consideration from a trivalent hexagonal lattice. Such a lattice is flat and has no vertex defects. In order to build a polyhedron we must introduce to it some curvature. By removing of a number of $\frac{\pi}{3}$ angles from the hexagonal lattice (see Fig. 1) and obtaining in this way an l-gonal face (in the centre of figure), the introduced curvature is

$$\gamma_l = (6 - l)\frac{\pi}{3}, \quad l = 1, 2, 3 \ldots \tag{5}$$

For $l = 3, 4, 5, 7$ the hexagonal face is replaced by an l-gon (triangle, square, pentagon, heptagon . . .). Subtituting (5) into the Gauss–Bonnet formula one again

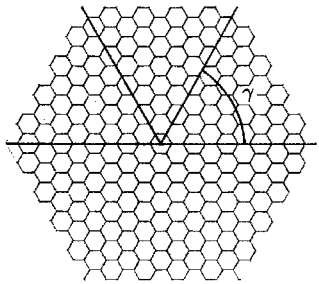

Fig. 1. The removal of the area inside the angle γ introduces the conical singularity.

gets the rule (3). As we can see, the number of hexagonal faces is, according to this rule arbitrary whereas the other types of faces must add up to the total curvature 4π. We will consider cages that are built only of hexagons and other types of l-gons with $l < 6$, therefore, we omit the cages containing, e.g., heptagons or other l-gons with $l > 6$, which introduce negative curvature. Such cages can also have spherical topology but are not convex. Note also that the cages having "faces" with $l = 2, 1$ are also conceivable. The faces are in these cases reduced to a single edge or even a vertex. The overview of these "regular" cages with the topology of a sphere is listed in the table ahead.

3. TETRAHEDRALLY SYMMETRIC (3,6) CAGES

One of the possible types of convex hexagonal cages are those containing only hexagonal and triangular faces. These cages, according to the Euler–Poincaré theorem, must contain exactly four triangular faces (cf. Fig. 2). The general theory will be presented at the end of this chapter, but now, for simplicity we start our considerations from tetrahedrally symmetric cages of that type. Such a cage can be created, geometrically, by adequate gluing of the edges of a triangular patch, like the one presented in Fig. 3. It is fully defined by one of the edge vectors, e.g., **A**, since the remaining two must lie at $\pi/3$ angles to the first one.

$$\begin{aligned} \mathbf{A} &= 2m\mathbf{T}_1 + 2n\mathbf{T}_2, \\ \mathbf{B} &= 2(m+n)\mathbf{T}_2 - 2n\mathbf{T}_1, \end{aligned} \tag{6}$$

where m and n are integers. A folded tetrahedron would look like the molecule on Fig. 4. The number of nodes, or lattice sites, in the cage is

$$N = 4(m^2 + n^2 + mn). \tag{7}$$

The first Brillouin zone is generated by

$$\mathbf{P}_1 = \frac{2\pi}{\sqrt{3}}\mathbf{e}_x - \frac{2\pi}{3}\mathbf{e}_y, \quad \mathbf{P}_2 = \frac{4\pi}{3}\mathbf{e}_y. \tag{8}$$

Overview of different hexagonal cages

l	1	2	3	4	5	6	7	...	
γ_i	$5\pi/3$	$4\pi/3$	π	$2\pi/3$	$\pi/3$	0	$-\pi/3$	...	
n_i					12	n			(5,6) fullerenes
					12	20			truncated icosahedron
					12+i	n	i		not convex cages
				6		n			(4,6) cages
				6		8			truncated octahedron
				5	2	n			
	•	•	•	•	•	•	•	•	family of **6** types of cages
				1	10	n			
			4			n			(3,6) cages
			4			4			truncated tetrahedron
			3	1	1	n			
	•	•	•	•	•	•	•	•	family of **12** types of cages
			1		9	n			
		3				n			(2,6) cages
		2	1		1	n			
	•	•	•	•	•	•	•	•	family of **15** types of cages
		1			8	n			
	2			1		n			(there are no (1,6) cages)
	2				2	n			
	•	•	•	•	•	•	•	•	family of **11** types of cages
	1				7	n			
									45 types of convex cages

Fig. 2. Classification of trivalent cages of genus 0.

Knowing this, we shall now show how to determine the electron wave function on the tetrahedron, using the covering function.

The simplest way of obtaining the wave functions of the tetrahedral cage is the adaptation of the wave functions of graphene and choosing only those which obey the boundary conditions characteristic for the cage, which are

$$\begin{aligned}
\psi(t\mathbf{A}) &= \psi(\mathbf{A} - t\mathbf{A}),\\
\psi(t\mathbf{B}) &= \psi(\mathbf{B} - t\mathbf{B}),\\
\psi(\mathbf{A} + t(\mathbf{B} - \mathbf{A})) &= \psi(\mathbf{B} + t(\mathbf{A} - \mathbf{B})),\\
\mathbf{n} \cdot \nabla\psi(t\mathbf{A}) &= -\mathbf{n} \cdot \nabla\psi(\mathbf{A} - t\mathbf{A}),\\
\mathbf{n} \cdot \nabla\psi(t\mathbf{B}) &= -\mathbf{n} \cdot \nabla\psi(\mathbf{B} - t\mathbf{B}),\\
\mathbf{n} \cdot \nabla\psi(\mathbf{A} + t(\mathbf{B} - \mathbf{A})) &= \mathbf{n} \cdot \nabla\psi(\mathbf{B} + t(\mathbf{A} - \mathbf{B})),
\end{aligned} \tag{9}$$

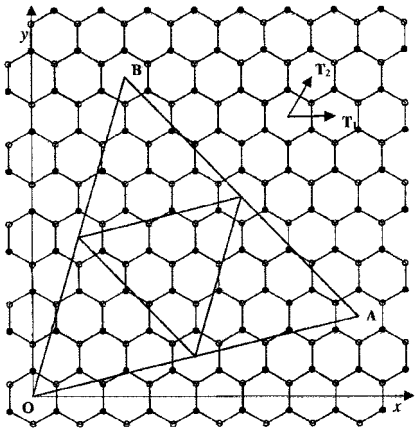

Fig. 3. The tetrahedron unfolded on the honeycomb plane.

where $0 \leq t < 1/2$. To obtain a function obeying the conditions (9) we construct a global wave function, defined on the whole graphene lattice, which is periodic in two period vectors **A** and **B**:

$$\Psi(\mathbf{r}) = \Psi(\mathbf{r} + i\mathbf{A} + j\mathbf{B}), \tag{10}$$

where i, j are integers. In addition this wave function should be invariant under the inversion:

$$\Psi(\mathbf{r}) = \Psi(-\mathbf{r}). \tag{11}$$

One can show (Ceulemans *et al.*, 2002) that any function obeying (10) and (11), when restricted to the triangle *OAB* automatically obeys (9), and therefore

$$\Psi|_{OAB}(\mathbf{r}) = \psi(\mathbf{r}). \tag{12}$$

In this way we can find arbitrary wave functions of the cluster. The wave functions of graphene are of the type (Ceulemans *et al.*, 2002):

$$|y\mu\mathbf{k}\rangle = c_{\mu k}^{(1)}|\mathbf{k}\rangle_1 + c_{\mu k}^{(2)}|\mathbf{k}\rangle_2, \tag{13}$$

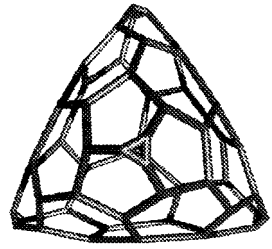

Fig. 4. An example of a tetrahedral cage.

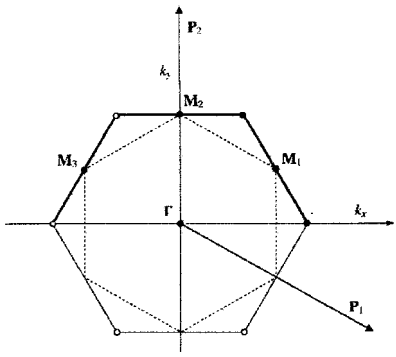

Fig. 5. The Brillouin zone of graphene, with its four special points — Γ corresponding to the $E = -3\gamma$ singlet state, M_1, M_2, and M_3 to the $E = \gamma$ triplet states.

where

$$|\mathbf{k}\rangle_1 = \frac{1}{\sqrt{N}} \sum_p \exp(i s_p \mathbf{r}_p \cdot \mathbf{k}) a_p^\dagger |0\rangle,$$

$$|\mathbf{k}\rangle_2 = \frac{1}{\sqrt{N}} \sum_p \exp(-i s_p \mathbf{r}_p \cdot \mathbf{k}) a_p^\dagger |0\rangle, \tag{14}$$

$\mu = 1, 2$ is the band index, $s_p = 1$ for black and $s_p = -1$ for blanc atoms. The periodicity condition (10) is satisfied provided

$$\mathbf{k} \cdot \mathbf{A} = 2\pi l_1,$$

$$\mathbf{k} \cdot \mathbf{B} = 2\pi l_2. \tag{15}$$

The allowed momentum vectors[2] read:

$$k_x = \frac{4\pi}{\sqrt{3} a N}[(m+n)l_1 - n l_2],$$

$$k_y = \frac{4\pi}{3 a N}[(n-m)l_1 + (2m+n)l_2]. \tag{16}$$

The energy spectrum for the tetrahedral cage is now easily obtained by inserting these vectors into the graphene dispersion relation. It has been shown (Dresselhaus *et al.*, 2001) that for carbon structures of not very large curvature the use of planar dispersion relation is well justified.

The eigenvalues of the two bands $\mu = 1, 2$ are

$$E_{\mu \mathbf{k}} = \alpha + (-1)^\mu \gamma \left(1 + 4\cos^2 \frac{\sqrt{3}}{2} k_x + 4 \cos \frac{\sqrt{3}}{2} k_x \cos \frac{3}{2} k_y\right)^{1/2}. \tag{17}$$

[2] Since the wave vectors are proportional to the momentum, we shall refer to **k** as the momentum vector.

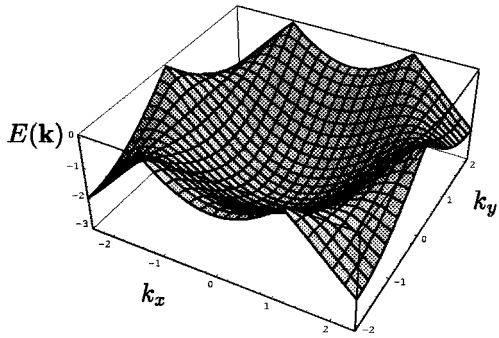

Fig. 6. The plot of the dispersion relation (Eq. (17)) for the graphene lattice.

The allowed values of momenta change depending on m and n (cf. Fig. 7). There are only four states in the first Brillouin zone, which are always allowed, independently of m and n; they are $\mathbf{\Gamma}$, $\mathbf{M}_1$, $\mathbf{M}_2$, and $\mathbf{M}_3$ (cf. Fig. 3). The point $\mathbf{\Gamma}$ corresponds to the lowest energy, -3γ and the $\mathbf{M}$ points to energy γ.

Apart from that, the spectrum is bipartite and symmertical with respect to $E = 0$. The wave vectors and resulting energy spectra for carbon tetrahedra of various edge vectors are shown on Fig. 7. Note that the spectra of both (4, 1) and (4, 4) tetrahedra include states at the Fermi level ($E = 0$), while the other do not. The presence of occupied states at the Fermi surface is a feature of all tetrahedra whose edge vectors satisfy the condition $(n - m)|_{mod3} = 0$, which we shall refer to as the metallicity condition. The construction above can be generalised to an arbitrary (3,6) cage. It is defined by four integer parameters m, n, p, and q, for the edge vectors, obeying the condition $mq - pn \neq 0$. The patch generating vectors are

$$\begin{aligned} \mathbf{A} &= 2m\mathbf{T}_1 + 2n\mathbf{T}_2, \\ \mathbf{B} &= 2p\mathbf{T}_1 + 2q\mathbf{T}_2. \end{aligned} \tag{18}$$

The procedure of obtaining the wave function of the cage from the graphene wave functions can be now applied, giving the following momentum vectors:

$$\begin{aligned} k_x &= \frac{\pi}{\sqrt{3}a}\frac{ql_1 + nl_2}{mq - pn}, \\ k_y &= \frac{\pi}{\sqrt{3}a}\frac{-(2p + q)l_1 + (2m + n)l_2}{mq - pn}. \end{aligned} \tag{19}$$

The allowed states in the reciprocal space display a symmetry lower than the one of the tetrahedron—they form a triangular lattice, but they are not equidistant, and the energy spectrum is not bipartite.

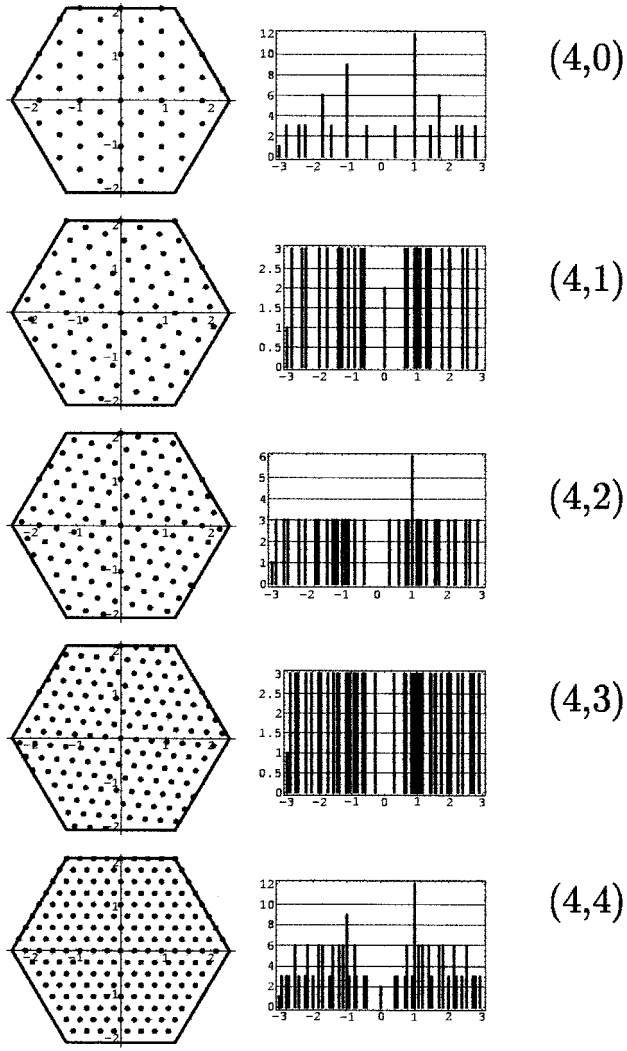

Fig. 7. The left column of plots represents the Brillouin zones of tetrahedra of various chiralities (the exact parameters are indicated at the far right). The right column shows their density of states plots.

Equations (19) and (17) fully determine the electronic properties of arbitrary (3, 6) cages. Figure 8 shows the patch of an arbitrary nontetrahedrally symmetrical (3,6) cage, Fig. 9 its first Brillouin zone and the energy spectrum.

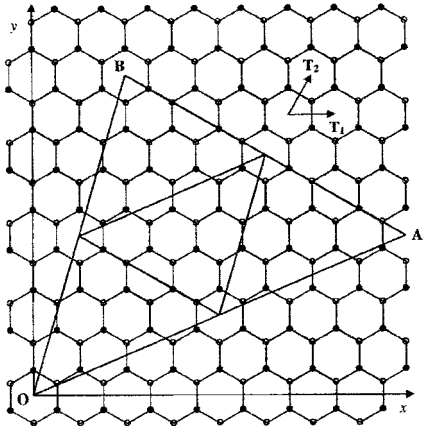

Fig. 8. The patch of a (3,6) cage, defined by parameters $m = 3$, $n = 2$, $p = -1$, $q = 4$.

4. PERSISTENT CURRENTS IN TOROIDAL GRAPHENE CAGES

The construction of a torus from a graphene patch is fully analogous to the construction of the tetrahedron, or a (3,6) cage. We can define again the two structural vectors, $\mathbf{L}_n = m_1\mathbf{T}_1 + m_2\mathbf{T}_2$, which stands for the circumference of a nanotube created after the first gluing, and $\mathbf{L}_t = p_1\mathbf{T}_1 + p_2\mathbf{T}_2$, standing for the length of this tube — which, upon the second gluing, becomes the circumference of the torus (we will call it simply the length of the torus). These two vectors do not have to be perpendicular. If they aren't, we have a twisted torus. When we insert the torus into an external magnetic field, parallel to the axis of the torus, the Aharonov–Bohm effect induces a shift in the phase of electronic states. This would be difficult to obtain analytically in the case of a tetrahedral cage but can be easily incorporated into the boundary conditions of a structure with rotational

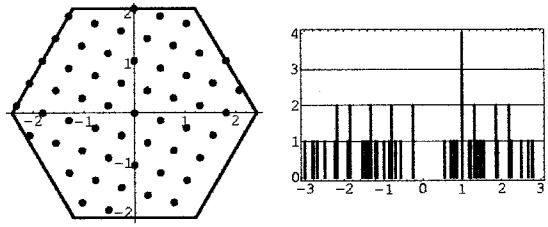

Fig. 9. Left: the Brillouin zone of a (3,2,–1,4) cage, note that points representing allowed momenta are not equidistant, contrary to the tetrahedron case. Right: density of states plot.

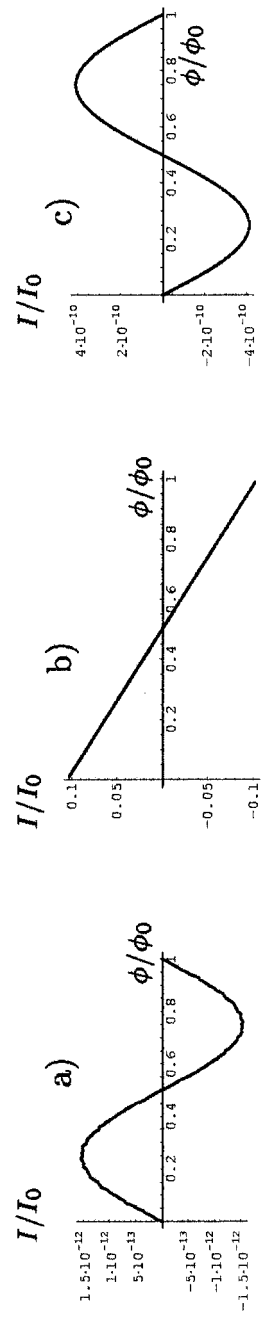

Fig. 10. The persistent currents at $T = 0$ in $I_0 = \gamma_e/h$ units, for three tori of similar length and twist: (a) $(7, 0) \times (-60, 120)$ – semiconducting, (b) $(7, 1) \times (-66, 120)$ – metallic, and (c) $(7, 3) \times (-78, 102)$ – semiconducting again. Note that the amplitude of the current in the case of the middle, metallic torus, is several orders of magnitude greater than in the two remaining cases.

symmetry (Lin and Chuu, 1998).

$$\mathbf{k} \cdot \mathbf{L}_n = 2\pi l_n,$$
$$\mathbf{k} \cdot \mathbf{L}_t = 2\pi(l_t + \phi/\phi_0), \quad \phi_0 = \frac{hc}{e} \tag{20}$$

where l_n and l_t are arbitrary integers, which results in the following equations for x and y momentum coordinates:

$$k_x = \frac{2\pi}{\sqrt{3}(m_1 p_2 - p_1 m_2)}(p_2 l_n + m_2(l_t + \phi/\phi_0)),$$
$$k_y = \frac{2\pi}{3(m_1 p_2 - p_1 m_2)}(-(2p_1 + p_2)l_n + (2m_1 + m_2)(l_t + \phi/\phi_0)). \tag{21}$$

Each of these allowed momentum states carries an electric current. Without the magnetic field the currents cancel out because of the Kramers degeneracy. When the magnetic field is switched on, the momentum coordinate along the torus ($k_t = \mathbf{k} \cdot \mathbf{L}_t/|\mathbf{L}_t|$) is modified. The currents don't cancel out any more and we obtain an overall topological current along the torus's circumference, called persistent because it runs without dissipation, as long as the magnetic field is present. This is a phenomenon common in systems of mesoscopic size, where the phase coherence length is of the same order of magnitude

5. FERMI LEVEL DEPENDENT CURRENTS IN CARBON NANOTUBES

The straight nanotubes, threaded by a magnetic flux, are more favourable for topological currents, since in their case some of the features that suppressed persistent currents in tori, are acting now in their favour. The magnetic field is applied along the axis of the tube, shifting states in the perpendicular direction. Since the states are more sparse in the direction in which they are shifted, the slope of the current is greater and the amplitude increases. Since the states are very dense along the axis of the tube, a large number of them corresponds to the same value of k_t and they are shifted together, thereby increasing the amplitude of the current again.

In zigzag nanotubes we can enhance the persistent currents even more, by lowering the Fermi level, i.e., hole-doping the tube. The $k_t = \text{const}$ lines are then exactly parallel to two sides of the Fermi surface (cf. Fig. 11) and the jump in the current is very large (cf. Fig. 12). As regards armchair nanotubes, the persistent currents decrease a few times with lowering the Fermi level to $-\gamma$ (Fig. 13), since the currents carried by states belonging to one momentum line are not correlated now. With these three modifications, the currents in hole-doped zigzag nanotubes can be much larger than in zigzag tori. They can attain values that would permit the existence of selfsustaining currents, however, this is a subject for further investigation.

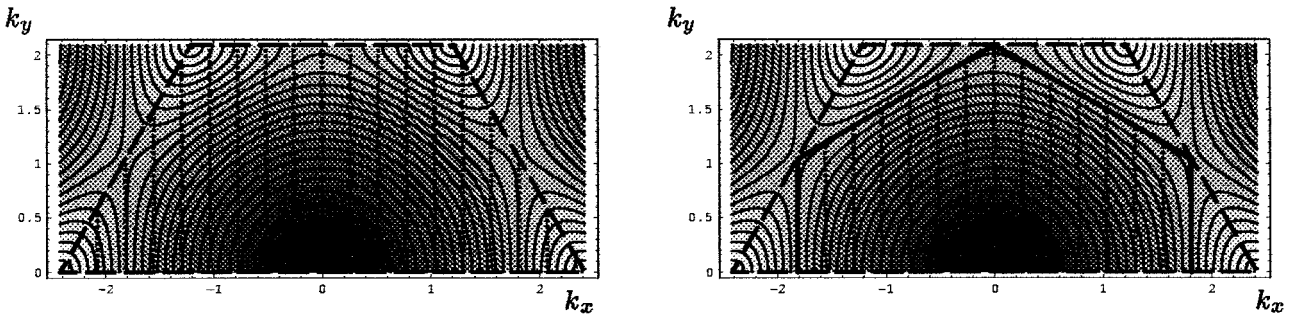

Fig. 11. The Brillouin zone at the half-filling (left) and at $E_F = -\gamma$ (right) of a $(14, 0) \times (-100, 200)$ nanotube. The background is the density plot of graphene dispersion relation, and the bold lines in the right picture denote the Fermi level.

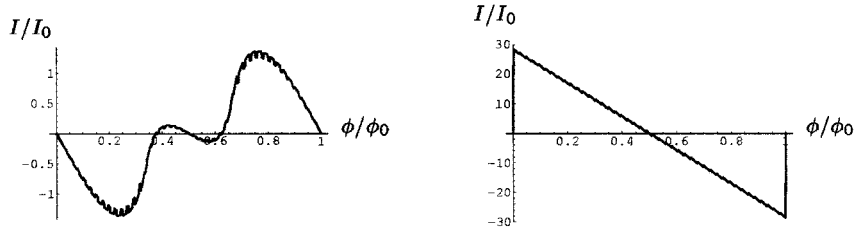

Fig. 12. The persistent current in $I_0 = \gamma_e/h$ units versus magnetic flux in $\phi_0 = hc/e$ units. Left: total persistent current in the $(14, 0) \times (-100, 200)$ nanotube at the half-filling; right: in hole-doped to the value of $E_F = -\gamma$.

6. CONCLUSIONS

Three different topological structures have been discussed by the use of a method of projecting a finite cluster onto the infinite space of a graphen lattice. The energy spectra for convex polyhedral cages, carbon tori, and carbon nanotubes were obtained by inserting the wave vectors obeying the appropriate boundary conditions, determined by the topology of the structure, into the graphene dispersion relation. We obtained the analytical energy spectra for all investigated systems, and in the case of tori and nanotubes, which have cylindrical symmetry, we could also examine their magnetic properties. The modification of wave vectors by the external magnetic flux results in persistent currents that are a hallmark of phase coherence. These currents strongly depend on the size of the systems and the details of their geometrical structure. We have shown that the amplitude of the currents is inversely proportional to the diameter of the system. The systems obeying the metallicity condition exhibit much larger currents (even by several orders of magnitude) than semiconducting systems of similar size. The twist of the nanotube forming a torus does not significantly influence the current.

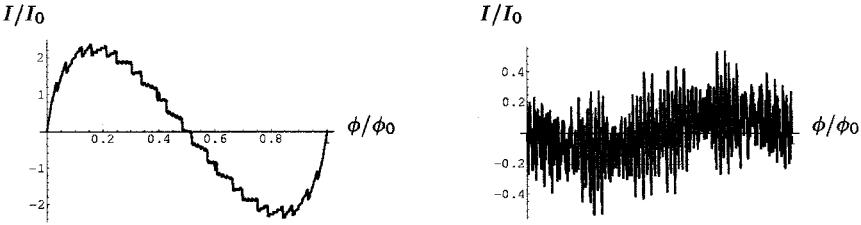

Fig. 13. Left: the persistent current in a half-filled armchair nanotube, $(9, 9) \times (-150, 150)$. Right: the same nanotube, but Fermi level lowered to $-\gamma$.

ACKNOWLEDGMENT

Work supported by the KBN Grant 2P03B 048 23.

REFERENCES

Ceulemans, A. *et al.* (2002). *Physical Review B* **65**, 115412.
Cheung, H. F., Gefen, Y., Riedel, E. K., and Shih, W. H. (1988). *Physical Review B* **37**, 6050;
Dresselhaus, M. S., Dresselhaus, G., and Avouris, P. (2001). *Carbon Nanotubes—Synthesis, Structure, Properties and Applications*, Springer, Berlin.
Fowler, P. W., John, P. E., and Sachs, H. (2000). *(3,6) Cages, Hexagonal Toroidal Cages and Their Spectra*, DIMACS Series in Discrete Math. Theoret. Comput. Sci., Vol. 51, pp. 139–174.
Gonzalez, J., Guinea, F., and Vozmediano, M. A. H. (1993). *Nuclear Physics B* **406**, 771.
Ijima, S. (1991). *Nature* **354**, 56.
Kroto H. W., Heath J. R., O'Brien S. C., Curland R. F., and Smalley R. E. (1985). *Nature* **318**, 162.
Lin, M. F. and Chuu, D. S. (1998). *Physical Review B* **57**, 6731.
Margańska, M. and Szopa, M. (2001). *Acta Physica Polonica* **32**, 427.
Szopa, M. (2001). *Symmetry and Structural Properties of Condensed Matter*, World Scientific, Singopore, p. 248.
Szopa, M., Margańska, M., and Zipper, E. (2002). *Physics Letters A* **299**.